Selective Molecular Transport through Intrinsic Defects in a Single Layer of CVD Graphene

Sean C. O'Hern,[†] Cameron A. Stewart,[†] Michael S. H. Boutilier,[†] Juan-Carlos Idrobo,[‡] Sreekar Bhaviripudi,[§] Sarit K. Das,[⊥] Jing Kong,[§] Tahar Laoui,[∥] Muataz Atieh,[∥] and Rohit Karnik[†,*]

[†]Department of Mechanical Engineering, Massachusetts Institute of Technology, Cambridge, Massachusetts 02139, United States, [‡]Materials Science and Technology Division, Oak Ridge National Laboratory, Oak Ridge, Tennessee 37831, United States, [§]Department of Electrical Engineering and Computer Science, Massachusetts Institute of Technology, Cambridge, Massachusetts 02139, United States, [⊥]Department of Mechanical Engineering, Indian Institute of Technology Madras, Chennai, India, and [∥]Departments of Mechanical and Chemical Engineering, King Fahd University of Petroleum and Minerals, Dhahran, Saudi Arabia

ABSTRACT

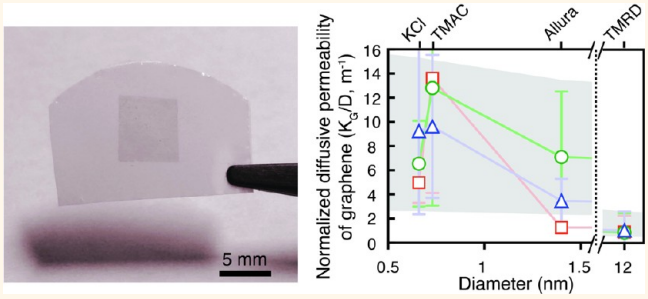

We report graphene composite membranes with nominal areas more than 25 mm^2 fabricated by transfer of a single layer of CVD graphene onto a porous polycarbonate substrate. A combination of pressure-driven and diffusive transport measurements provides evidence of size-selective transport of molecules through the membrane, which is attributed to the low-frequency occurrence of intrinsic 1−15 nm diameter pores in the CVD graphene. Our results present the first step toward the realization of practical membranes that use graphene as the selective material.

KEYWORDS: graphene membranes · nanofiltration · filtration · nanofluidics

Graphene, with its atomistic thickness,[1,2] remarkable mechanical strength,[3] and potential for size-selective transport through nanometer-scale holes in its lattice,[4−6] is an ideal material for next-generation membranes[7] with high selectivity and permeability. Although impermeable in its pristine state,[8] theoretical models predict that by the introduction of holes of controlled size, density, and functionalization, graphene membranes would outperform existing state-of-the-art membranes in gas-phase and liquid-phase separation processes by orders of magnitude in terms of permeability and selectivity.[5,9] However, experimental measurements of ionic and molecular transport through graphene membranes have so far been limited to microscopic areas. DNA translocation has been detected *via* measurement of ionic currents through single nanopores in suspended graphene,[10−12] while graphene nanoballoon measurements have demonstrated the impermeability of pristine graphene to gases including helium.[8] In contrast, voltage-driven ionic transport has been observed across small areas of suspended graphene grown by chemical vapor deposition (CVD), suggesting that it is permeable to ions,[12] although the origin of this phenomenon is unclear.

Much progress is required beyond the current status for exploiting the incredible potential of graphene to realize practical membranes, including advances in methods for fabricating large-area, nearly defect-free graphene on porous supports, generating a high density of controlled nanoscale pores, and better understanding of the relationship between the pore structures and transport properties. In contrast to multilayer graphene-based membranes that can be processed from bulk graphite,[13] practical membranes that employ flow across nanoscale pores in graphene are likely to be made from CVD graphene that can be grown over large areas at atmospheric pressure.[14,15] For realizing such membranes, it is important to develop methods to suspend graphene over macroscopic areas of a porous support and to investigate the permeability of CVD graphene to the transport of ions and molecules.

Here, we experimentally investigate the transport of ions and molecules across a single layer of large-area CVD graphene transferred to a porous polycarbonate track

* Address correspondence to karnik@mit.edu.

Received for review August 23, 2012 and accepted October 2, 2012.

Published online October 02, 2012
10.1021/nn303869m

etch (PCTE) membrane support. We develop a procedure to transfer graphene (~25 mm^2) to the PCTE membrane and characterize the coverage of the transferred graphene using pressure-driven flow. Through measurement of diffusive transport and scanning transmission electron microscopy, we show that the CVD graphene contains a low frequency of intrinsic holes that permit the selective transport of molecules. The measured permeability is consistent with predictions of continuum theory.

RESULTS AND DISCUSSION

Membrane Fabrication. We fabricated graphene composite membranes (GCM) to measure transport through a single layer of CVD graphene *via* transfer of large areas of graphene to a mechanically robust porous polymer support with minimal large holes or tears (Figure 1a). We used CVD graphene on copper, as it can be grown over large areas comprising primarily single layers.[14] While several methods have been developed to transfer or otherwise create suspended graphene membranes starting from CVD graphene on copper,[16−19] they typically require lithographic patterning or substrates capable of withstanding high temperatures or solvents. In contrast, the direct transfer procedure first reported by Regan *et al.*[20] is simple and compatible with polymeric supports and was therefore modified and adapted in this work for fabrication of the large-area GCMs.

Our scalable, direct-transfer process relies on the conformability of a porous polymer substrate to adhere to the graphene (on copper) *via* a simple pressing process followed by etching of the copper (Figure 1b). The porous polymer supports the graphene during the copper-etching phase and also gives it sufficient mechanical robustness for further handling. Before drying, the GCM was rinsed in an ethanol/water mixture to minimize mechanical stresses due to the receding meniscus. Although the process is amenable to any conformable, thin-film porous polymer support, we selected a PCTE membrane with 200 nm pores (Sterlitech) as our target substrate. The straight, cylindrical pores present a well-defined transport resistance for extraction of the intrinsic transport properties of graphene and provide adequate porosity while avoiding excessively large areas of free-standing graphene.

Since the transfer procedure relies on solid−solid adhesion between the PCTE membrane and the graphene, the resulting membrane quality is sensitive to variations in the transfer procedure that can influence the graphene−PCTE membrane contact. We found that the three primary factors that influence the quality of the transfer are the hydrophobicity of the substrate, the surface roughness of the copper on which the graphene is grown, and the type of etchant used to remove the copper.

The transfer procedure relies on the hydrophobicity of the substrate to keep the etchant from wetting the

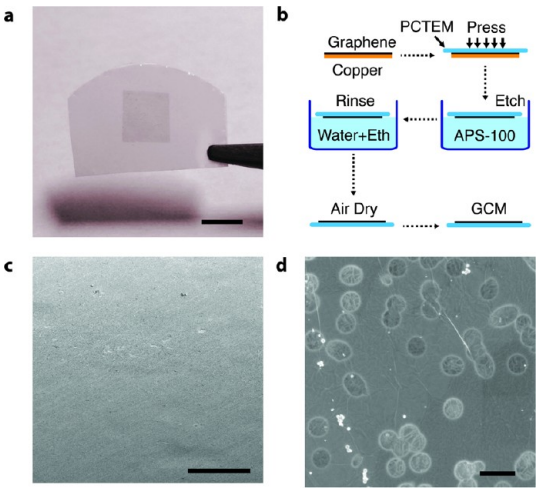

Figure 1. (a) Graphene composite membrane (GCM) consists of large-area graphene on polycarbonate track etch (PCTE) membrane. Scale bar is 5 mm. (b) Process developed to transfer low-pressure CVD graphene from copper foil to PCTE membrane to fabricate GCM. (c) Scanning electron microscope (SEM) image of a large area of high-quality graphene suspended over PCTE membrane pores (compare to Figure 2b for low-quality transfer). Scale bar is 100 μm. (d) Magnified SEM image of graphene suspended over PCTE membrane pores. Scale bar is 500 nm.

interface between the graphene and the substrate. Although polycarbonate is naturally hydrophobic, PCTE membranes are often coated with polyvinylpyrrolidone (PVP) to act as a wetting agent to enhance fluid flow for various applications. When PVP-coated PCTE membranes were tested during the transfer procedure, the interface between the PCTE membrane and the graphene-coated copper foil wetted almost immediately when floated on the surface of water or copper etchant (see Figure 2a), resulting in separation of the PCTE membrane and the graphene due to wicking of the solution. For this reason only PVP-free hydrophobic PCTE membranes were used.

As this transfer process relies on conformal contact between the polymer support and the graphene, the underlying topography of the copper foil directly affects the quality of the graphene transfer. Rolled copper typically has troughs due to the manufacturing process. As shown in Figure 2b, these troughs may lead to lines of cracks in the graphene on the copper due to nonconformal contact in these regions. The graphene initially used for the study was grown on copper with an rms surface roughness of 500 nm (Alfa Aesar, 0.025 mm, 99.8%, graphene grown using procedure developed by Li *et al.*[14]). The graphene used for the final experiments had an rms surface roughness of 185 nm, which eliminated the problem.

The type of etchant used was also found to greatly impact the quality of the transfer. When using a ferric chloride-based copper etchant (CE-100, Transene) to remove copper during the transfer procedure, many cracks appeared in the transferred graphene, spaced

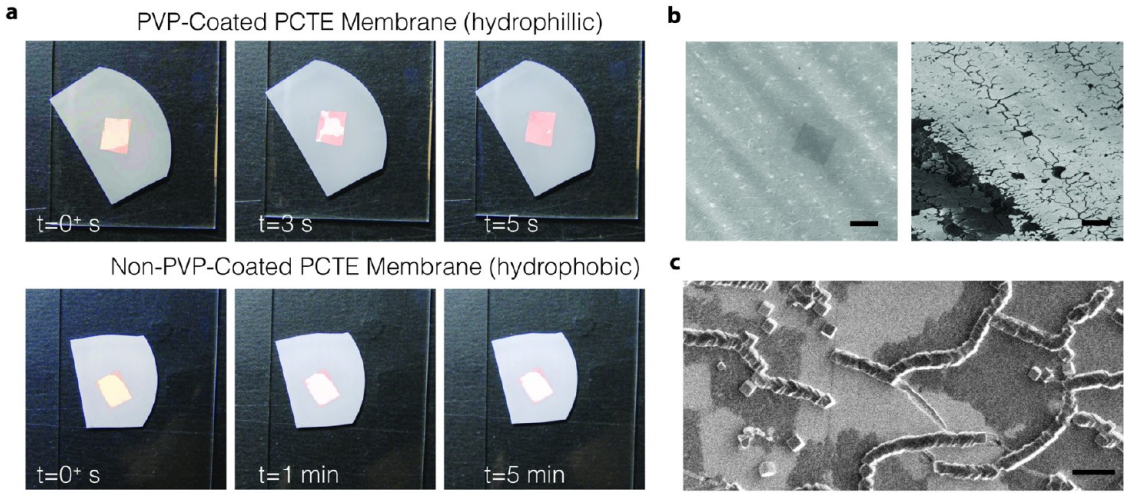

Figure 2. (a) As-synthesized graphene on copper floated on water after pressing against hydrophilic (PVP-coated) and hydrophobic (non-PVP-coated) polycarbonate track etch (PCTE) membranes. Wicking of the solution between the graphene and PCTE membrane appears as the darker copper color in the case of the PVP-coated membrane. (b) Corrugations in the as-synthesized graphene on copper appear as striations in the SEM images and result in nonconformal contact between the graphene and the PCTE membrane during transfer. This nonconformal contact results in a high density of cracks in the graphene on the PCTE membrane that appear as dark regions in the SEM images of the graphene composite membrane. The dark areas are regions not covered with graphene, whereas the light regions are covered with graphene. Scale bars are 10 μm. (c) SEM images of graphene on copper after 5 s exposure to CE-100 ($FeCl_3$ copper etchant). Crystalline products of the reaction tend to remain on the surface of the graphene and tear the graphene. Scale bar is 1 μm.

approximately the same distance apart as the graphene wrinkles that occur due to the differing thermal expansion coefficients of graphene and copper.[14] We hypothesized that crystallization of the poorly soluble copper(I) chloride produced by the etching reaction may lead to tearing of the graphene along grain boundaries, defects, or wrinkles.[21] We placed a single drop of the CE-100 etchant on a graphene-coated copper foil, rinsed it after 5 s, and observed it using SEM. Crystals resulting from the reaction were clearly seen on the surface of the graphene (see Figure 2c), also indicating that the underlying copper was accessible to the etchant. Although the etchant attacks the copper from the other side during the actual transfer process, the force of crystallization[22] has the potential to tear apart the graphene in the final stages of etching if the products of the reaction are not quickly removed from the surface. To eliminate this problem, an ammonium persulfate-based etchant (APS-100, Transene) was used instead of CE-100. The products of this reaction are water-soluble copper(II) sulfate, which eliminates the issue of crystal growth during etching. This was confirmed *via* SEM, which did not reveal any crystal formation on the surface after a similar drop test (see Figure 5c).

The best quality GCMs were thus obtained using the smoother copper and etching it with APS-100 under moderate pressure to increase gas solubility and minimize the possibility of bubble nucleation on the suspended graphene.[23,24] When imaged in a SEM, cracks and tears manifested as dark regions, often with bright outlines, when compared to unbroken sections of graphene.[25] Typical defects in the GCM were

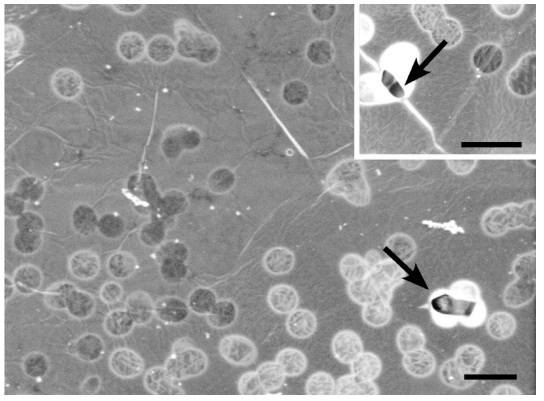

Figure 3. Uncovered single polycarbonate track etch membrane pores (indicated by arrows) and cracks (inset) were two types of defects commonly found in graphene after transfer. Analysis of similar images revealed typical graphene coverage to be 90−98%. Scale bars are 500 nm.

single-pore defects, possibly intrinsic or due to the formation of trapped gas nanobubbles on the surface of the graphene due to outgassing of the APS-100, and cracks, either intrinsic to the graphene or introduced during the transfer procedure (Figure 3). Of the ~25 mm^2 area transferred, image analysis revealed that 90−98% of the area was typically covered with graphene, depending on the particular transfer.

Transport Measurements. To further confirm the coverage, we measured convective pressure-driven flow of water through the GCM. The GCM was mounted in a Side-bi-Side diffusion cell (Permgear, Inc.), and the flow rate was measured using UV−vis spectrophotometry when water (with a dissolved tracer dye) flowed out into a reservoir (Figure 4a). Since convective pressure-driven

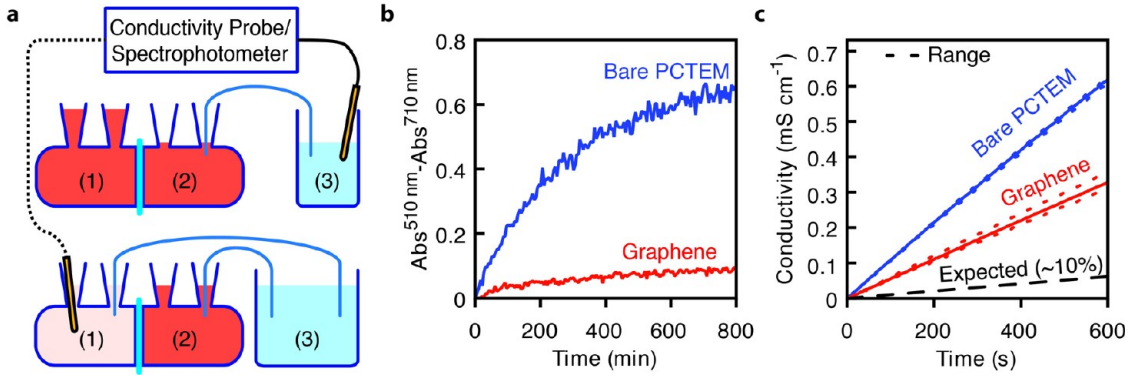

Figure 4. Convective and diffusive transport measurements reveal good coverage during transfer and permeability of CVD graphene to KCl. (a) (Top) Gravitational pressure head drives convective transport of 1 mM Allura Red AC solution from bath (1) through graphene composite membrane to bath (2), which then travels through tubing to bath (3) to equalize liquid level. Change in absorbance in bath (3) measured *via* a UV−vis spectrophotometer is used to extract the flow rate. (Bottom) Concentration gradient drives diffusion of solute (*e.g.*, KCl) from bath (2) through GCM to bath (1). Change in conductivity (for salts) or absorbance (for organic molecule solutes) in bath (1) is measured *via* a UV−vis spectrophotometer or conductivity meter. To ensure minimal convective transport, baths (1) and (2) are maintained at a constant liquid level through a connected large external bath (3) for solutes with low diffusivity. (b) Convective transport through GCM (M1) is ∼10% that of the bare PCTE membrane (PCTEM), indicating ∼90% graphene coverage in GCM. The slope of the curve for the bare PCTEM decreases as the meniscus level drops. (c) Diffusive transport rate of KCl through GCM (M1) is 46% that of the transport through the bare PCTEM, much higher than the expected value of ∼10% if the graphene were impermeable. Dashed lines denote the range of data in three different experiments on the membrane (M1).

flow rate scales as D^4/L for a cylindrical PCTE pore of diameter D and length L (as opposed to D^2/L for diffusive transport), comparison of the pressure-driven flow rate of the GCM with the PCTE membrane allowed us to directly measure the coverage of graphene on the PCTE membrane. Accounting for the known geometry (200 nm diameter, ∼10 μm length) of the PCTE membrane pores, we estimate that any hole or tear in the graphene larger than ∼50 nm in diameter will provide little resistance to flow and will be counted as an open PCTE membrane pore, whereas smaller holes in graphene will obstruct the flow of water (see Supporting Information). We find graphene coverage of 88% to 93% for the three GCMs, denoted by M1, M2, and M3, fabricated for this study (Figure 4b), which agrees with the SEM characterization and confirms the integrity of the GCMs after mounting in the diffusion cell.

Next, we measured the diffusion of potassium chloride (KCl) through the GCM by introducing 0.5 M KCl and deionized water on opposite sides of the GCM and monitoring the conductivity change in the deionized water. The solutions were vigorously stirred to eliminate the effects of concentration polarization in the vicinity of the membrane (Figure S2). The measured rates of diffusive transport through the bare PCTE membrane agreed well with those calculated from the known membrane pore geometry and porosity (see Figure S5). If graphene were defect-free and impermeable to KCl, *i.e.*, no pores or tears smaller than ∼50 nm, a ∼10% diffusive flux would be expected compared to a PCTE membrane without graphene. Contrary to our expectations, for the three GCMs M1, M2, and M3, we observed a KCl transport rate in the range 46−71% of that through the PCTE membrane without graphene (see Figure 4c for transport through M1 and Table S2), which suggested that the CVD graphene was permeable to KCl.

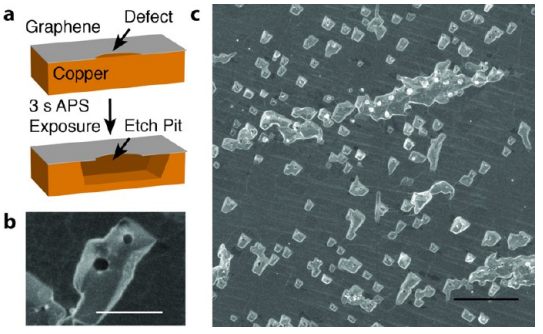

Figure 5. (a) Reaction between APS-100 and graphene-coated copper occurs only at defect sites in the graphene and results in etch pits in the underlying copper. (b) Etch pit in copper under suspended graphene after exposure to APS-100 copper etchant for 3 s. Scale bar is 0.5 μm. (c) Surface of graphene on copper after exposure to APS-100 for 3 s indicates the density of defects in the graphene surface. Scale bar is 2 μm.

Intrinsic Holes in CVD Graphene. Tests with placing a drop of CE-100 copper etchant on graphene-coated copper revealed that the etchant can access the copper (Figure 2c). Similarly, we also placed a drop of APS-100 on the surface of the as-synthesized graphene on copper for 3 s, then rinsed in DI water.[26] SEM images clearly indicate that discrete holes in the graphene permit the APS-100 to leak past the graphene barrier and react with the copper underneath, resulting in suspended regions of graphene (Figure 5). However, this process was difficult to control, and many of the observed holes resulted from dislodging of sporadic amorphous particles that have been previously observed

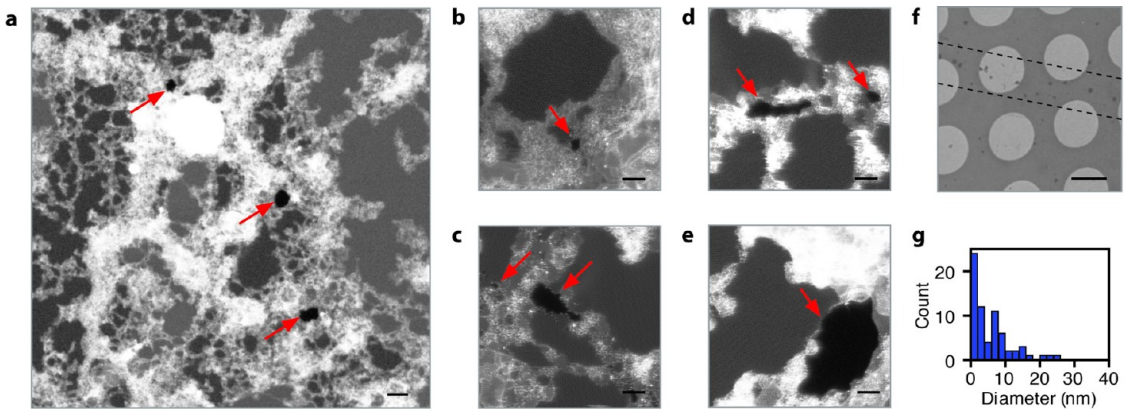

Figure 6. Characterization of nanometer-scale pores in graphene by STEM medium-angle annular dark field (MAADF). (a) Low density of pores can be seen in the graphene lattice, as indicated by red arrows. Scale bar is 10 nm. (b−e) Representative images of pores that vary in size from 1 to 15 nm in diameter. Scale bars are 2 nm. (f) A higher concentration of pores exists in the region between the dashed lines. Scale bar is 1 μm. (g) Distribution of pore sizes imaged in STEM suggests ~83% of holes in lattice are less than 10 nm in diameter.

to form on the graphene surface.[26] To characterize the pore size distribution more accurately, we examined the graphene lattice structure using aberration-corrected scanning transmission electron microscopy (STEM). The electron microscope was operated at 60 kV to avoid any electron beam damage. To enable STEM imaging, graphene was transferred to a TEM grid[20] using APS-100 as the copper etchant. We discovered that, unlike pristine graphene, the low-pressure CVD graphene contained pores in the size range of 1−15 nm that appear to be distributed in a pattern analogous to the features on the copper foil used for CVD synthesis (Figure 6). While the origin of these pores is not understood, their existence is consistent with the expected lower quality of CVD graphene compared to pristine graphene from highly oriented pyrolytic graphite and observations of ionic transport across CVD graphene.[12]

We also investigated whether the pore defects are intrinsic or are created or enlarged by the APS copper etchant during the transfer process. Reports suggest that graphene is more susceptible to oxidation in amorphous regions, grain boundaries, and intrinsic point defects.[27,28] Raman spectroscopy of graphene exposed to APS (an oxidizer) revealed increasing D and D′ bands that suggest creation of defects in the lattice (Figure S4). However, it was observed that the permeability of graphene to KCl did not increase with APS exposure. There was little difference between 5 min or 1 h exposures; an increase in transport rates was not obtained even after 3 days of exposure (Figure S4), suggesting that while APS may modify the graphene, it was not able to significantly enlarge existing defects or nucleate new pores in graphene. The results suggest that intrinsic defects during the growth of graphene on copper were responsible for the nanometer-scale pores.

Size-Selective Transport through CVD Graphene. The existence of intrinsic defects in graphene is expected to result in size-selective transport, where molecules larger than the pore size are excluded. Therefore, we measured the diffusive transport of molecular species of increasing sizes across the GCM: KCl, tetramethylammonium chloride (TMAC), Allura Red AC (496 Da dye), and tetramethylrhodamine dextran (70 kDa, TMRD). In the case of Allura Red and TMRD, which have low diffusivities, pressure gradients across the membrane during transport measurements were eliminated by fluidically connecting both sides to an external reservoir. Three different membranes were fabricated for this purpose; the diffusive transport for all molecules was measured in triplicate for the first membrane, and pressure-driven tests for measurement of graphene coverage and KCl transport tests (see Figure 4) were performed after each measurement to ensure consistency of the results. Since the results were repeatable in the first membrane (M1) and required ~3−4 weeks for triplicate measurements, transport through the other two membranes (M2 and M3) was measured only once, and errors were estimated from the reproducibility of the measurements on the first membrane. We found that the GCMs permitted transport of KCl and TMAC, but blocked the diffusion of the 70 kDa TMRD (Figure 7a). Compared to the PCTE membrane, the GCM resulted in ~80−85% decrease in the diffusive flux of TMRD, which is consistent with the pore size distribution (Figure 6g) and graphene coverage measured using pressure-driven flow (Figure 4b).

Diffusive Permeability of CVD Graphene. The well-defined geometry of the membranes enables estimation of the transport properties of graphene by modeling the composite membrane as a circuit and assuming spatial homogeneity as a first approximation (see Supporting Information) (Figure 7b). We can estimate the diffusive permeability of graphene, K_G (m s^{-1}), as

$$K_G = \left[A_T \varepsilon \Delta C \left(\frac{1-\eta}{\dot{n}_{GCM} - \eta j_{PC} A_T} - \frac{1}{j_{PC} A_T} \right) \right]^{-1} \quad (1)$$

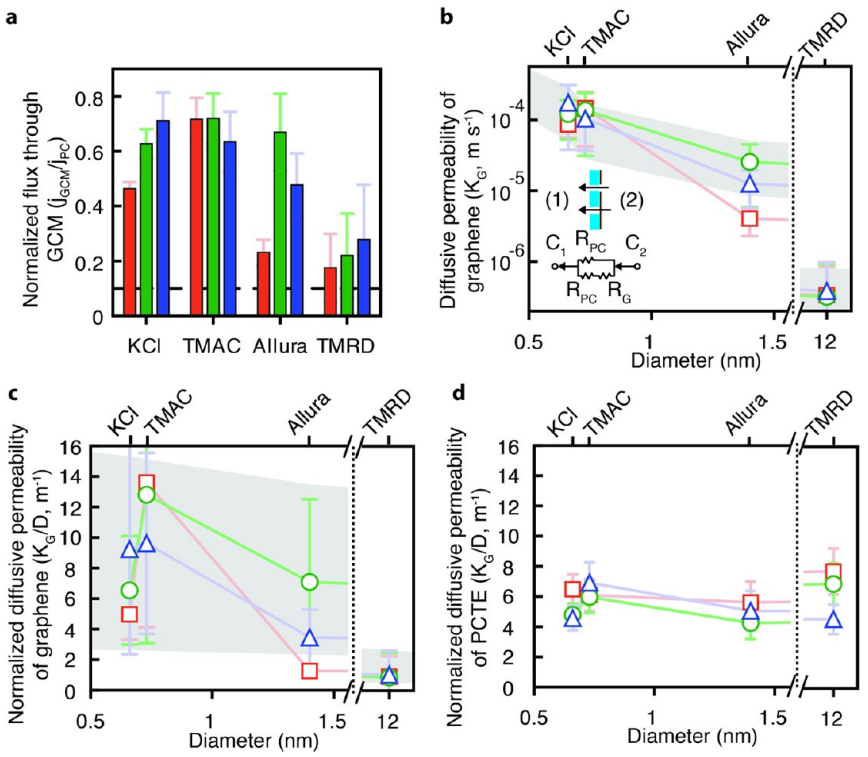

Figure 7. Size-selective diffusion of molecules through graphene membranes. (a) Diffusive flux of molecules through GCM normalized by that through unmodified polycarbonate track etch (PCTE) membranes for three different GCMs (M1 is red, M2 is green, and M3 is blue in all panels). Dashed line represents the flux expected for 90% graphene coverage on the PCTE membrane if the graphene is impermeable to the molecules. (b) Permeability of the CVD graphene, K_G, calculated for the three membranes using a simple circuit model (inset), indicated as a function of the diameters of the molecules (hydrated diameters for the salts and Stokes–Einstein diameters for Allura and TMRD). C_1 and C_2 denote concentrations, while R_{PC} and R_G denote resistance to diffusive transport of a PCTE membrane pore and graphene covering a single PCTE membrane pore, respectively. Only two pores, one of which is covered by graphene, are shown for clarity. The gray region denotes the continuum model prediction for graphene of porosity between 0.025% and 0.15%. (c) Permeability of graphene normalized by the diffusivity of the molecule indicates that the transport of the 12 nm diameter TMRD molecule was significantly attenuated compared to the smaller molecules. Gray region denotes continuum model prediction with the same porosity range as in (b). (d) Measured permeability of the PCTE membrane normalized by the diffusivity does not exhibit any selectivity as expected. Error bars indicate 95% confidence. If no error bars are present, error is within the range of the symbol.

where ΔC is the driving concentration difference, A_T is the membrane area, η is one less the fractional graphene coverage on the PCTE membrane, $\dot{n}_{GCM}$ is the molar flow through the graphene composite membrane, j_{PC} is the molar flux through the bare PCTE membrane, and ε is the PCTE membrane porosity (see Supporting Information). Using this model, the open pores in the PCTE membrane (*i.e.*, those without any graphene coverage or with holes in graphene >50 nm in diameter) are accounted for and the transport properties of graphene can be extracted. The absolute permeabilities extracted from the model exhibit a monotonically decreasing trend, as is expected due to the lower diffusivities of the larger species (Figure 7b). The uncertainly in these estimates arises primarily from the variability in PCTE membrane geometry and partly from the uncertainty in the estimated coverage of graphene (see Supporting Information). To account for the different diffusivities of each molecular species, the permeability is normalized by the diffusivity (Figure 7c). The results clearly illustrate that the diffusive transport of the larger TMRD molecules is attenuated by about 1 order of magnitude compared to the smaller species. The Stokes–Einstein molecular diameters of Allura Red and TMRD are ~1 and ~12 nm, respectively, suggesting that the majority of the pores are between 1 and 10 nm in size, which is consistent with the STEM observations.

Knowing the pore size distribution of the intrinsic pores in graphene (Figure 6g), we used continuum theory for diffusion across isolated pores in a thin membrane to estimate the diffusive permeability, K_G, of graphene for a species of radius H, which is given by (see Supporting Information):

$$K_G = 2D\gamma \sum_{a_i>H} (a_i - H) / \sum_{a_i} \pi a_i^2 \qquad (2)$$

Here, D is the species diffusivity, a_i is the pore radius, γ is the graphene porosity (ratio of graphene pore area to graphene area, which accounts for pores smaller than ~50 nm), and the summation is over the pore size distribution. While the pore size distribution is known (Figure 6g), using pore number density measurements from STEM imaging and exposure of graphene-coated copper to etchant, the porosity was estimated to lie

between 0.61% and 0.012% (see Supporting Information). The permeability predicted by eq 2 shows good agreement with the measured permeability for γ in the range 0.025−0.15% (chosen to fit the data and indicated by the gray area in Figure 7b, c), which is consistent with the porosity estimates. The agreement between the experimentally measured permeability and the continuum theory further indicates that the observed transport behavior is due to the nanometer-scale pores in the graphene.

CONCLUSION

In this work, we fabricated membranes comprising a single sheet of CVD graphene on a porous support and developed methods to measure the transport properties of graphene. The results presented here demonstrate that it is possible to achieve selective molecular transport through macroscopic areas of single sheets of CVD graphene and, as such, are a first step toward utilizing the full potential of graphene for advancing membrane technologies. The understanding of the origins of the permeability of graphene and the measurement techniques developed in this study will aid the design of future graphene membranes for various applications and may also provide insights into the behavior of graphene as barrier films.[29] The transport of molecules through these intrinsic defects as well as larger defects formed during the membrane fabrication process will certainly need to be minimized, or at least controlled, for the development of such membranes. While nucleation and growth of graphene on copper and formation of grains is fairly well understood,[30,31] little is known about pore defects that occur during this process. Our study shows that these defects occur at a fairly low frequency, and we can only speculate that they occur due to defects in the copper itself or deposition and growth of particulates on the copper. Improvements in the quality of CVD graphene through the optimization of gas flow rates, reduction of surface roughness,[32] and the use of high-purity copper may reduce the occurrence of intrinsic defects. Additionally, improvements in the membrane fabrication process will reduce the occurrence of leaks through areas that are not covered by graphene. For pressure-driven separations, appropriate choice of the resistance of the porous support to fluid flow so that it matches that of the graphene will further minimize the magnitude of any flow that bypasses the selective graphene layer and will thereby enable the effects of intrinsic defects and leaks to be minimized; other approaches may include stacking of graphene layers to minimize leaks. Further progress in understanding and controlling the size, number density, and functional groups of pores in graphene during its synthesis, through chemical treatment, or by other means[33−36] promises to reveal interesting transport properties for applications in gas separations, water purification, and biomedicine. Finally, we anticipate that advances in graphene manufacturing technologies driven in part by the demand for electronic and other applications will facilitate the realization of practical, high-quality, and high-performance graphene membranes.

MATERIALS AND METHODS

Materials. Low-pressure CVD graphene on 25 μm copper foil was purchased commercially from ACS Materials and characterized *via* Raman spectroscopy (see Supporting Information) unless otherwise mentioned. Copper etchants used for transfers were APS-100 (10−20% ammonium persulfate, Transene) and CE-100 (25−35% iron(III) chloride, Transene). Target substrates for graphene transfers were Sterlitech non-PVP coated, hydrophobic, polycarbonate track etch membranes with 200 nm pores and gold 200 mesh Quantifoil holey carbon transmission electron microscope grids (Ted Pella, Inc.) with 1.2 μm diameter holes. Dyes and salts used in transport experiments were potassium chloride (Mallinckrodt Chemicals), tetramethylammonium chloride (Sigma-Aldrich), 80% (for pressure-driven flow experiments) and 98% (for diffusive transport experiments) Allura Red AC (Sigma-Aldrich), and 70 kDa tetramethylrhodamine dextran (Life Technologies).

PCTE Membrane Device Fabrication. For transport measurements, as-synthesized low-pressure CVD graphene on copper (ACS Materials) was transferred to PCTE membranes (Sterlitech) with 200 nm pores using a simple pressing procedure. After cutting to size (~25 mm^2), the graphene on the backside of the copper was removed by floating in APS-100 for 7 min, then rinsed in two subsequent water baths for 10 min each. After drying, the sample was placed on weigh paper atop a glass slide. The PCTE membrane was placed on top of the graphene, and a second glass slide was placed on top of the stack. The whole stack was then pressed with light finger pressure using a pipet tube as a rolling pin. The pressure caused the pliable PCTE membrane to conform to the contours of the copper, adhering the PCTE membrane to the graphene. The PCTE membrane-supported graphene on copper was then transferred to a bath of APS-100 etchant and etched under 7 psi (gauge) for 5 min beyond the full removal of the copper. Afterward, the sample was removed, rinsed in a water bath, followed by a 50% ethanol/water bath, and finally air-dried.[23]

Scanning Electron Microscopy. All SEM images were carried out on a Helios Nanolab Dualbeam 600 (Center for Materials Science and Engineering, MIT) at 1−5 kV and 86 pA to 0.22 nA. Low-magnification images were captured in secondary electron mode with an Everhart-Thornley SE detector. To decrease the effect of charging in the polymer substrate and to enhance the resolution of graphene, the samples were tilted to 52° unless otherwise noted. For high-magnification imaging (Figure 1d, Figure 3, and Figure 5b, c), samples were imaged in immersion mode with a 0° tilt.

Scanning Transmission Electron Microscopy. All STEM imaging was performed on a Nion UltraSTEM 100,[37] which is part of the Share Research Equipment (ShaRE) user facility at Oak Ridge National Laboratory. The microscope was operated with an acceleration voltage of 60 kV to ensure that no damage would be done to the graphene while imaging. Images were acquired using a medium-angle annular dark field detector with ~54 to 200 mrad half-angle range. Before imaging, the samples were baked for 10 h under 10^{-5} Torr at 160 °C to decrease surface contamination. After cooling to room temperature under vacuum for about 10 h, they were immediately transferred to the STEM column.

The images were filtered using a low-pass smoothing function implemented in the program ImageJ, and the s-curve of the image was adjusted in Adobe Photoshop to increase the contrast between the graphene lattice and the holes.

Transport Measurements. Transport measurements were carried out using a 3.4 mL Side-bi-Side glass diffusion cell with a 3 mm orifice (Permegear, Inc.). To wet the membrane after insertion in the diffusion cell, both sides of the cell were filled with 50% ethanol/water, then rinsed thoroughly using degassed DI water. During each transport measurement, the solution in each side was stirred with Teflon stir bars to minimize concentration polarization. Both sides of the cell were rinsed thoroughly with DI water after each experiment.

For pressure-driven transport measurements, one side of the cell was filled with 3 mL of 1 mM 80% Allura Red AC/0.5 M KCl solution, while the other was filled with 4 mL of the same solution. The side with less solution was connected to an external bath containing 16.7 mL of 0.5 M KCl with 20 cm tubing of 0.5 mm inner diameter. The height of the solution in this external bath was matched to the height of dye solution in the diffusion cell. The volume difference between the two sides resulted in a 14 mm height difference, thereby generating a pressure gradient across the membrane. As dye flowed from the 4 mL side to the 3 mL side, the dye solution flowed through the tubing to the external bath as the height between the bath and 3 mL side equalized. The change in absorbance spectrum of the external bath was measured using a Cary 60 UV−vis spectrophotometer with a fiber optic dip probe.

Salt diffusion experiments were carried out using 0.5 M KCl (Mallinckrodt Chemicals) or 0.5 M TMAC (Sigma-Aldrich). One side of the diffusion cell was filled with 3.25 mL of DI water, and the other was filled with 3.25 mL of the salt solution. An eDAQ Conductivity isoPod with a miniature dip-in conductivity electrode was placed in the water side of the diffusion cell and captured the conductivity every second for 12 min. Organic molecule diffusion experiments were carried out using 1 mM 98% Allura Red AC (Sigma-Aldrich) or 0.417 mg/mL TMRD (Life Technologies) in 0.5 M KCl. To ensure diffusion-dominated transport, both sides of the diffusion cell were connected using 20 cm of 0.5 mm i.d. tubing to an external bath containing 0.5 M KCl. The UV−vis spectrophotometer probe was placed in the 0.5 M KCl side of cell, and an absorbance spectrum from 800 to 200 nm was obtained every 15 s for 1 h or until a steady change in the absorbance spectrum was observed.

To take into account possible drift over the course of the organic dye experiments (both pressure-driven transport and diffusive transport), the concentration of the organic solution was calculated by taking the difference between two points on the absorbance spectrum with one point corresponding to a peak in absorbance and the other corresponding to a point independent of concentration. Observed absorbance peaks occurred at 510 nm for Allura Red AC and 515 nm for TMRD. The concentration-independent point used for both species was 710 nm.

Conflict of Interest: The authors declare no competing financial interests.

Acknowledgment. The authors would like to thank N. Hadjiconstantinou, T. Jain, and J. Lee for helpful discussions regarding this work and K. Mullen for assisting in graphene transfers. This work was funded by King Fahd University of Petroleum and Minerals in Dhahran, Saudi Arabia, through the Center for Clean Water and Clean Energy at MIT and KFUPM under project number R10-CW-09. The research was also supported by ORNL's Shared Research Equipment (ShaRE) User Program (J.C.I.), which is sponsored by the Office of Basic Energy Sciences, U.S. Department of Energy. Research was performed in part at the Center for Nanoscale Systems (CNS), a member of the National Nanotechnology Infrastructure Network, which is supported by the National Science Foundation under NSF award no. ECS-0335765. CNS is part of Harvard University. This research was also performed in part at the Center for Materials Science and Engineering at MIT.

Supporting Information Available: Additional methods, supplementary data, theoretical modeling, and data analysis are included. This material is available free of charge *via* the Internet at http://pubs.acs.org.

REFERENCES AND NOTES

1. Allen, M. J.; Tung, V. C.; Kaner, R. B. Honeycomb Carbon: A Review of Graphene. *Chem. Rev.* **2010**, *110*, 132–145.
2. Geim, A. Graphene: Status and Prospects. *Science* **2009**, *324*, 1530–1534.
3. Lee, C.; Wei, X.; Kysar, J.; Hone, J. Measurement of the Elastic Properties and Intrinsic Strength of Monolayer Graphene. *Science* **2008**, *321*, 385–388.
4. Du, H.; Li, J.; Zhang, J.; Su, G.; Li, X.; Zhao, Y. Separation of Hydrogen and Nitrogen Gases with Porous Graphene Membrane. *J. Phys. Chem. C* **2011**, *115*, 23261–23266.
5. Jiang, D.; Cooper, V.; Dai, S. Porous Graphene as the Ultimate Membrane for Gas Separation. *Nano Lett.* **2009**, *9*, 4019–4024.
6. Suk, M.; Aluru, N. Water Transport through Ultrathin Graphene. *J. Phys. Chem. Lett.* **2010**, *1*, 1590–1594.
7. Humplik, T.; Lee, J.; O'Hern, S.; Fellman, B.; Baig, M.; Hassan, S.; Atieh, M.; Rahman, F.; Laoui, T.; Karnik, R.; *et al*. Nanostructured Materials for Water Desalination. *Nanotechnology* **2011**, *22*, 292001.
8. Bunch, J.; Verbridge, S.; Alden, J.; van der Zande, A.; Parpia, J.; Craighead, H.; McEuen, P. Impermeable Atomic Membranes from Graphene Sheets. *Nano Lett.* **2008**, *8*, 2458–2462.
9. Cohen-Tanugi, D.; Grossman, J. Water Desalination across Nanoporous Graphene. *Nano Lett.* **2012**, *12*, 3602–3608.
10. Merchant, C.; Healy, K.; Wanunu, M.; Ray, V.; Peterman, N.; Bartel, J.; Fischbein, M.; Venta, K.; Luo, Z.; Johnson, A.; *et al*. DNA Translocation through Graphene Nanopores. *Nano Lett.* **2010**, *10*, 2915–2921.
11. Schneider, G.; Kowalczyk, S.; Calado, V.; Pandraud, G.; Zandbergen, H.; Vandersypen, L.; Dekker, C. DNA Translocation through Graphene Nanopores. *Nano Lett.* **2010**, *10*, 3163–3167.
12. Garaj, S.; Hubbard, W.; Reina, A.; Kong, J.; Branton, D.; Golovchenko, J. Graphene as a Subnanometre Trans-Electrode Membrane. *Nature* **2010**, *467*, 190–193.
13. Nair, R.; Wu, H.; Jayaram, P.; Grigorieva, I.; Geim, A. Unimpeded Permeation of Water Through Helium-Leak-Tight Graphene-Based Membranes. *Science* **2012**, *335*, 442–444.
14. Li, X.; Cai, W.; An, J.; Kim, S.; Nah, J.; Yang, D.; Piner, R.; Velamakanni, A.; Jung, I.; Tutuc, E.; *et al*. Large-Area Synthesis of High-Quality and Uniform Graphene Films on Copper Foils. *Science* **2009**, *324*, 1312–1314.
15. Luo, Z.; Lu, Y.; Singer, D.; Berck, M.; Somers, L.; Goldsmith, B.; Johnson, A. Effect of Substrate Roughness and Feedstock Concentration on Growth of Wafer-Scale Graphene at Atmospheric Pressure. *Chem. Mater.* **2011**, *23*, 1441–1447.
16. Reina, A.; Jia, X.; Ho, J.; Nezich, D.; Son, H.; Bulovic, V.; Dresselhaus, M.; Kong, J. Layer Area, Few-Layer Graphene Films on Arbitrary Substrates by Chemical Vapor Deposition. *Nano Lett.* **2009**, *9*, 3087–3087.
17. Lin, Y.; Jin, C.; Lee, J.; Jen, S.; Suenaga, K.; Chiu, P. Clean Transfer of Graphene for Isolation and Suspension. *ACS Nano* **2011**, *5*, 2362–2368.
18. Lee, C.; Kim, B.; Ren, F.; Pearton, S.; Kim, J. Large-Area Suspended Graphene on GaN Nanopillars. *J. Vac. Sci. Technol. B* **2011**, *29*, 060601.
19. Aleman, B.; Regan, W.; Aloni, S.; Altoe, V.; Alem, N.; Girit, C.; Geng, B.; Maserati, L.; Crommie, M.; Wang, F.; *et al*. Transfer-Free Batch Fabrication of Large-Area Suspended Graphene Membranes. *ACS Nano* **2010**, *4*, 4762–4768.
20. Regan, W.; Alem, N.; Aleman, B.; Geng, B.; Girit, C.; Maserati, L.; Wang, F.; Crommie, M.; Zettl, A. A Direct Transfer of Layer-Area Graphene. *Appl. Phys. Lett.* **2010**, *96*, 113102.
21. Pereira, V.; Neto, A.; Liang, H.; Mahadevan, L. Geometry, Mechanics, and Electronics of Singular Structures and Wrinkles in Graphene. *Phys. Rev. Lett.* **2010**, *105*, 156603.
22. Weyl, P. K. Pressure Solution and the Force of Crystallization - A Phenomenological Theory. *J. Geophys. Res.* **1959**, *64*, 2001–2025.

23. O'Hern, S. C. Development of Process to Transfer Large Areas of LPCVD Graphene from Copper Foil to a Porous Support Substrate. Thesis (M.S), Massachusetts Institute of Technology, Cambridge, MA, 2011.
24. Yang, S.; Dammer, S.; Bremond, N.; Zandvliet, H.; Kooij, E.; Lohse, D. Characterization of Nanobubbles on Hydrophobic Surfaces in Water. *Langmuir* **2007**, *23*, 7072–7077.
25. Suk, J.; Kitt, A.; Magnuson, C.; Hao, Y.; Ahmed, S.; An, J.; Swan, A.; Goldberg, B.; Ruoff, R. Transfer of CVD-Grown Monolayer Graphene onto Arbitrary Substrates. *ACS Nano* **2011**, *5*, 6916–6924.
26. Hofmann, M. Advances in the CVD Growth of Graphene for Electronics Applications. Ph.D. Thesis, Massachusetts Institute of Technology, Cambridge, MA, 2012.
27. Liu, L.; Ryu, S.; Tomasik, M.; Stolyarova, E.; Jung, N.; Hybertsen, M.; Steigerwald, M.; Brus, L.; Flynn, G. Graphene Oxidation: Thickness-Dependent Etching and Strong Chemical Doping. *Nano Lett.* **2008**, *8*, 1965–1970.
28. Nemes-Incze, P.; Yoo, K.; Tapaszto, L.; Dobrik, G.; Labar, J.; Horvath, Z.; Hwang, C.; Biro, L. Revealing the Grain Structure of Graphene Grown by Chemical Vapor Deposition. *Appl. Phys. Lett.* **2011**, *99*, 023104.
29. Prasai, D.; Tuberquia, J.; Harl, R.; Jennings, G.; Bolotin, K. Graphene: Corrosion-Inhibiting Coating. *ACS Nano* **2012**, *6*, 1102–1108.
30. Batzill, M. The Surface Science of Graphene: Metal Interfaces, CVD Synthesis, Nanoribbons, Chemical Modifications, and Defects. *Surf. Sci. Rep.* **2012**, *67*, 83–115.
31. Mattevi, C.; Kim, H.; Chhowalla, M. A Review of Chemical Vapour Deposition of Graphene on Copper. *J. Mater. Chem.* **2011**, *21*, 3324–3334.
32. Han, G.; Gunes, F.; Bae, J.; Kim, E.; Chae, S.; Shin, H.; Choi, J.; Pribat, D.; Lee, Y. Influence of Copper Morphology in Forming Nucleation Seeds for Graphene Growth. *Nano Lett.* **2011**, *11*, 4144–4148.
33. Tracz, A.; Wegner, G.; Rabe, J. Scanning Tunneling Microscopy Study of Graphite Oxidation in Ozone-Air Mixtures. *Langmuir* **2003**, *19*, 6807–6812.
34. Bai, J.; Zhong, X.; Jiang, S.; Huang, Y.; Duan, X. Graphene Nanomesh. *Nat. Nanotechnol.* **2010**, *5*, 190–194.
35. Wu, S.; Yang, R.; Shi, D.; Zhang, G. Identification of Structural Defects in Graphitic Materials by Gas-Phase Anisotropic Etching. *Nanoscale* **2012**, *4*, 2005–2009.
36. Russo, C. J.; Golovchenko, J. A. Atom-By-Atom Nucleation and Growth of Graphene Nanopores. *Proc. Natl. Acad. Sci. U. S. A.* **2012**, *109*, 5953–5957.
37. Krivanek, O.; Corbin, G.; Dellby, N.; Elston, B.; Keyse, R.; Murfitt, M.; Own, C.; Szilagyi, Z.; Woodruff, J. An Electron Microscope for the Aberration-Corrected Era. *Ultramicroscopy* **2008**, *108*, 179–195.